



Cite this: *Phys. Chem. Chem. Phys.*, 2022, 24, 17496

## Photoelectron spectroscopy of cryogenically cooled $\text{NiO}_2^-$ via slow photoelectron velocity-map imaging<sup>†</sup>

Mark C. Babin, <sup>‡</sup><sup>a</sup> Martin DeWitt, <sup>a</sup> Jascha A. Lau, <sup>a</sup> Marissa L. Weichman, <sup>§</sup><sup>a</sup> Jongjin B. Kim, <sup>a</sup> Lan Cheng <sup>\*b</sup> and Daniel M. Neumark <sup>\*ac</sup>

High-resolution anion photoelectron spectra of cryogenically cooled  $\text{NiO}_2^-$  anions, obtained using slow photoelectron velocity-map imaging (cryo-SEVI), are presented in tandem with coupled cluster electronic structure calculations including relativistic effects. The experimental spectra encompass the  $\tilde{\chi}^1\Sigma_g^+ \leftarrow \tilde{\chi}^2\Pi_g$ ,  $\tilde{\alpha}^3\Pi_g \leftarrow \tilde{\chi}^2\Pi_g$ , and  $\tilde{\Lambda}^1\Pi_g \leftarrow \tilde{\chi}^2\Pi_g$  photodetachment transitions of linear  $\text{ONIO}^{0/-}$ , revealing previously unobserved vibrational structure in all three electronic bands. The high-resolution afforded by cryo-SEVI allows for the extraction of vibrational frequencies for each state, consistent with those previously measured in the ground state and in good agreement with scalar-relativistic coupled-cluster calculations. Previously unobserved vibrational structure is observed in the  $\tilde{\alpha}^3\Pi_g$  and  $\tilde{\Lambda}^1\Pi_g$  states and is tentatively assigned. Further, a refined electron affinity of 3.0464(7) eV for  $\text{NiO}_2$  is obtained as well as precise term energies for the  $\tilde{\alpha}$  and  $\tilde{\Lambda}$  states of  $\text{NiO}_2$  of 0.3982(7) and 0.7422(10) eV, respectively. Numerous Franck–Condon forbidden transitions involving the doubly degenerate  $\nu_2$  bending mode are observed and ascribed to Herzberg–Teller coupling to an excited electronic state.

Received 27th May 2022,  
Accepted 7th July 2022

DOI: 10.1039/d2cp02396b

rsc.li/pccp

### I. Introduction

Nickel oxides are an important class of catalytic materials with a wide range of industrial applications including the formation of syngas,<sup>1,2</sup> oxidative dehydrogenation of alkanes,<sup>3,4</sup> and carbon monoxide oxidation.<sup>5</sup> Therefore, understanding their properties is of both technological and fundamental importance. While much of the emphasis of nickel oxide catalysis involves condensed phase experiments, the gas phase study of isolated mass-selected metal oxide clusters provides a complementary molecular-level understanding of the structure and reactivity of these species.<sup>6,7</sup> Here, we report high-resolution anion photoelectron spectra of cryogenically cooled  $\text{NiO}_2^-$ , revealing a

wealth of vibronic structure throughout the three lowest-lying electronic states of  $\text{NiO}_2$ .

There are relatively few experimental studies concerning the structure<sup>8–12</sup> and reactivity of  $\text{NiO}_2^{0/-}$ .<sup>13–16</sup> Neutral  $\text{NiO}_2$  was first studied in gas matrices, where three isomers were identified in an Ar matrix:<sup>9</sup> cyclic  $\text{Ni}(\text{O}_2)$ , bent  $\text{NiOO}$ , and linear  $\text{ONIO}$  (referred to as  $\text{NiO}_2$  hereafter). Subsequent work in Ne matrices found preferential formation of  $\text{NiO}_2$  with trace  $\text{Ni}(\text{O}_2)$ , allowing for the extraction of two and three vibrational frequencies for these species, respectively.<sup>12</sup> In the gas phase, anion photoelectron spectroscopy (PES) has been used to probe the geometric and electronic structure of these species. The first PES study of  $\text{NiO}_2^-$  was performed by Wu and coworkers,<sup>10</sup> who observed photodetachment from both the bent  $\text{Ni}(\text{O}_2)$  and linear  $\text{NiO}_2$  anions, finding the electron affinity (EA) of  $\text{Ni}(\text{O}_2)$  to be 0.82(3) eV, considerably lower than that of  $\text{NiO}_2$  at 3.05(1) eV. The  $\text{NiO}_2$  band showed partially resolved vibrational structure with a frequency of  $750\text{ cm}^{-1}$ . This work also found transitions to two low-lying electronic states of  $\text{NiO}_2$  with term energies of 0.40(2) and 0.77(3) eV. Subsequent anion PES work performed by Ramond *et al.*<sup>11</sup> reexamined the ground state spectrum of  $\text{NiO}_2$  with improved resolution, yielding a refined EA of 3.043(5) eV as well as the  $\nu_1$  symmetric stretch frequency of 745(30)  $\text{cm}^{-1}$  from a progression in this mode.

The electronic and vibrational structure of  $\text{NiO}_2$  pose a considerable challenge to theory owing to its multireference nature.<sup>17,18</sup>

<sup>a</sup> Department of Chemistry, University of California, Berkeley, CA 94720, USA.

E-mail: dneumark@berkeley.edu

<sup>b</sup> Department of Chemistry, Johns Hopkins University, Baltimore, Maryland 21218, USA. E-mail: lcheng24@jhu.edu

<sup>c</sup> Chemical Sciences Division, Lawrence Berkeley National Laboratory, Berkeley, CA 94720, USA

<sup>†</sup> Electronic supplementary information (ESI) available. See DOI: <https://doi.org/10.1039/d2cp02396b>

<sup>‡</sup> Current address: Department of Chemistry and Chemical Biology, Harvard University, 12 Oxford St, Cambridge, MA 02138, USA.

<sup>§</sup> Current address: Department of Chemistry, Princeton University, Princeton, New Jersey 08544, USA.

<sup>¶</sup> Current address: KLA Corporation, 1 Technology Dr, Milpitas, CA 95035.

Treatments using density functional theory,<sup>9,12,19–21</sup> coupled cluster methods,<sup>21</sup> and multireference methods<sup>22</sup> have found a  $\Sigma_g^+$  ground electronic term for linear  $\text{NiO}_2$  that lies 0.7–1.5 eV below the  $\text{Ni}(\text{O}_2)$  structure. In both structures, there are numerous low-lying singlet and triplet species calculated to reside within ~2 eV of the ground state. The most definitive of these works is a joint multiconfiguration self-consistent field (MCSCF) and multireference configuration interaction (MRCI) study by Hübner,<sup>22</sup> which finds a  $^1\Sigma_g^+$  ground state with  $^3\Pi_g$  and  $^1\Pi_g$  states lying 0.537 and 0.943 eV higher in energy, in good agreement with the observed term energies from anion PES. Less work has been done on the  $\text{NiO}_2^-$  anion, with an early DFT study by Gustev *et al.*<sup>20</sup> finding a  $^2\text{A}_2$  bent ground state and more recent DFT work by Deng and coworkers<sup>19</sup> finding a linear  $^2\Pi_g$  ground state.

Here, we utilize slow electron velocity-map imaging spectroscopy of cryogenically-cooled anions (cryo-SEVI), a high-resolution variant of anion photoelectron spectroscopy, to study the photodetachment of  $\text{NiO}_2^-$ . In this method, cold ions are detached with a tunable laser and the resultant electron kinetic energy distribution is analyzed by a velocity-map imaging (VMI) spectrometer that is optimized for the detection of slow electrons, yielding photoelectron spectra with sub-meV resolution.<sup>23,24</sup> Revisiting the photoelectron spectra of  $\text{NiO}_2^-$  with cryo-SEVI provides substantial improvements in resolution over previous work. Beyond well-resolved vibrational structure in the ground and excited states, we observe a number of Franck–Condon (FC)-forbidden transitions in the ground state that display behavior distinct from that of the FC-allowed transitions near the photodetachment threshold. These features are ascribed to vibronic coupling to an excited electronic state. Our findings are supported by scalar-relativistic coupled-cluster calculations, with computed term energies and vibrational frequencies in good agreement with our observed spectra.

## II. Experimental methods

The cryo-SEVI method has been described in detail previously.<sup>23,25,26</sup> Here,  $\text{NiO}_2^-$  anions are formed *via* laser ablation using a rotating and translating nickel disk onto which a frequency-doubled Nd:YAG is focused. The resulting plasma is entrained within a pulse of He carrier gas from an Even-Lavie solenoid valve,<sup>27</sup> with residual  $\text{O}_2$  in this carrier gas serving to form  $\text{NiO}_2^-$  as it passes through a narrow channel to foster collisional cooling and cluster formation. The ions then pass through a skimmer before entering a radiofrequency (RF) hexapole ion guide and RF quadrupole mass filter that direct them into a linear RF octupole ion trap held at 5 K and filled with a buffer gas mixture of 20 : 80  $\text{H}_2$  : He. Collisions with this cold buffer gas mixture result in effective vibrational, rotational, and electronic cooling of the ions, leading to internal temperatures of around 10 K.<sup>26,28–30</sup>

The ions are held approximately 40 ms in the trap before being extracted into an orthogonal Wiley–McLaren time-of-flight mass spectrometer<sup>31</sup> and focused into the interaction region of a standard three-plate Eppink–Parker VMI electrostatic

lens assembly.<sup>32</sup> In the VMI spectrometer, the ions are photo-detached using the frequency-doubled output of a dye laser pumped by the second harmonic of a Nd:YAG laser operating at 20 Hz.

The resulting photoelectrons are projected onto a 2D detector comprising two chevron-stacked microchannel plates coupled to a phosphor screen, which is photographed by a CCD camera after each laser shot.<sup>33</sup> Each image is analyzed for individual electron events for which the centroids are calculated and binned into a  $1024 \times 1024$  grid.<sup>34</sup> The three-dimensional electron velocity distribution is reconstructed from the accumulated images using an inverse-Abel method.<sup>35</sup> The radial position of features in the reconstructed image is related to electron kinetic energy (eKE) by acquiring VMI images for detachment from atomic  $\text{F}^-$  at several photon energies.<sup>36</sup>

The VMI spectrometer has an approximately constant resolving power,  $\Delta\text{eKE}/\text{eKE}$ ,<sup>32</sup> yielding the highest eKE resolution for slow photoelectrons. As such, a SEVI spectrum is acquired by first taking an overview spectrum at a sufficiently high photon energy to access all (or most) of the photodetachment transitions before tuning the detachment laser to energies slightly above features of interest. This procedure results in the collection of high-resolution spectra over narrow energy windows that are then concatenated and scaled to match intensities in the overview spectrum, which is less sensitive to variation of the photodetachment cross section with photon energy. Spectra are plotted as a function of electron binding energy (eBE), given by  $\text{eBE} = h\nu - \text{eKE}$ .

## III. Computational methods

Electronic structure calculations for the  $\tilde{\chi}^2\Pi_g$  state of  $\text{NiO}_2^-$  and the  $\tilde{\chi}^1\Sigma_g^+$  state of  $\text{NiO}_2$  have been carried out at the coupled-cluster singles doubles augmented with a noniterative triples [CCSD(T)]<sup>37</sup> level of theory to determine the equilibrium structures and the harmonic vibrational frequencies of these states as well as to enable Franck–Condon simulation for the electron detachment transitions from the electronic ground state of  $\text{NiO}_2^-$  to that of  $\text{NiO}_2$ . Scalar-relativistic effects have been taken into account using spin-free exact two-component theory in its one-electron variant (SFX2C-1e)<sup>38,39</sup> together with the aug-cc-pVTZ basis set<sup>40–42</sup> recontracted for SFX2C-1e calculations. Calculations using a hierarchy of CC methods including CCSD,<sup>43</sup> CC singles doubles triples (CCSDT),<sup>44,45</sup> and CC singles doubles triples quadruples (CCSDTQ)<sup>46,47</sup> have also been performed for the  $\tilde{\chi}^1\Sigma_g^+$  state of  $\text{NiO}_2$  to examine the reliability of the CCSD(T) results, as this state exhibits strong electron-correlation effects.<sup>17,18</sup> The results of this analysis are outlined in Table S1 of the ESI.† Harmonic frequency calculations have been performed by means of numerical differentiation of analytically evaluated gradients using the analytic-gradient techniques for the CC methods and the SFX2C-1e scheme as implemented in the CFOUR program package.<sup>48–55</sup> FC simulations presented here employ the double-harmonic approximation using the fcsquared module<sup>56</sup> of the CFOUR program.

We have also performed SFX2C-1e equation-of-motion coupled-cluster singles doubles (EOM-CCSD)<sup>57</sup> and EOM-CC singles doubles triples (EOM-CCSDT)<sup>58,59</sup> calculations to determine the excitation energies of  $\text{NiO}_2^-$  in the anionic equilibrium structure. These are combined with the computed vertical detachment energy for the ground  $\tilde{\chi}^1\Sigma_g^+$  state of  $\text{NiO}_2^-$  to describe the vertical detachment energies from the ground state of  $\text{NiO}_2^-$  to these excited states of  $\text{NiO}_2^-$ . Here, aug-cc-pVQZ basis sets were used for EOM-CCSD calculations. The triples corrections have been obtained as the differences between EOM-CCSDT and EOM-CCSD results using cc-pVQZ basis sets. All calculations have been performed using the CFOUR program package,<sup>53,55</sup> except that the EOM-CCSDT calculations of triplet excited states have been carried out using the MRCC program package.<sup>60–62</sup>

## IV. Results and discussion

The cryo-SEVI spectrum of  $\text{NiO}_2^-$  is presented in Fig. 1. Fig. 1a shows the lower-eBE region of structure, spanning 24 400–28 000  $\text{cm}^{-1}$  and covering the ground state band of the  $\text{NiO}_2^- \leftarrow \text{NiO}_2^-$  photodetachment transition previously observed.<sup>10,11</sup> The higher-energy region of the spectra shown in Fig. 1b spans 27 550–32 500  $\text{cm}^{-1}$  and encompasses detachment transitions to excited electronic states of  $\text{NiO}_2^-$  as will be discussed in Sections IV.A and IV.D. In both figures, a low-resolution overview spectrum (blue) is displayed above high-resolution composite spectra (black) taken at several photon energies.

These spectra represent a significant improvement over previous anion photoelectron spectroscopy studies.<sup>10,11</sup> The improved resolution afforded by the cryo-SEVI method reveals not only the electronic transitions to the three lowest-lying states of  $\text{NiO}_2^-$  (features A1, C1, D1, respectively) previously observed, but also a manifold of transitions to vibrationally excited states of the neutral species. Peak assignments, electron binding energies (eBEs), as well as shifts from peak A1 are presented in Tables 1–3, while extracted experimental parameters are presented in Table 4.

In the case of the  $\text{NiO}_2^-$  ground state band, assignments of features are facilitated by our SFX2C-1e-CCSD(T)/aug-cc-pVQZ calculations, which allow for FC simulations to be performed for detachment transitions terminating in the  $\tilde{\chi}^1\Sigma_g^+$  state of  $\text{NiO}_2^-$ . This simulated spectrum facilitates the definitive vibrational assignments in this state and suggests vibrational assignments for the  $\tilde{\alpha}$  and  $\tilde{\Lambda}$  states of  $\text{NiO}_2^-$ . Notably, there are several strong transitions (B1–17) observed in this spectrum that are not reproduced by our simulations. Moreover, these features (B1–B5, for example) are clearly not present in the overview spectrum and retain considerable intensity near detachment threshold. This trend is depicted in Fig. 2, in which spectra collected at three photon energies highlight the differing behavior of these features as the photodetachment threshold is approached. As discussed in Section IV.C, our assignments for the B peaks all involve odd changes of vibrational quanta in

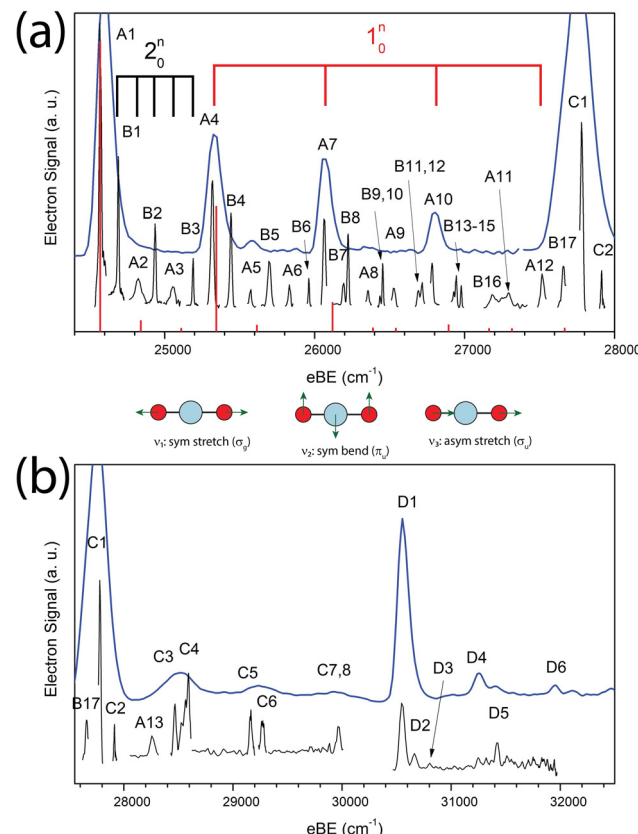


Fig. 1 Cryo-SEVI spectra of  $\text{NiO}_2^-$  showing detachment to the (a)  $\tilde{\chi}^1\Sigma_g^+$  ground state and (b)  $\tilde{\alpha}^3\Pi_g$  and  $\tilde{\Lambda}^1\Pi_g$  excited states. Blue traces are low-resolution overview scans taken with photon energies of 30 394 and 35 025  $\text{cm}^{-1}$  for panels (a) and (b), respectively. Black traces are high-resolution scans taken at variable photon energies, while red stick spectra in (a) represent FC simulations for the  $\tilde{\chi}^1\Sigma_g^+ \leftarrow \tilde{\chi}^2\Pi_g$  photodetachment transition from  $\text{NiO}_2^-$ . Vibrational modes for the ground state are depicted below the ground-state spectrum.

the non-totally symmetric  $\nu_2$  bending mode and are hence Franck–Condon forbidden.

Vibrational frequencies were not calculated for the two observed excited states of  $\text{NiO}_2^-$ , though the even spacing of levels and intensity patterns in the cryo-SEVI spectra lend themselves to tentative assignments to different vibrational levels of these two states of  $\text{NiO}_2^-$  (Section IV.D).

### IV.A Computational results

Our coupled-cluster calculations confirm that the electronic ground state of  $\text{NiO}_2$  is the  $\chi^1\Sigma_g^+$  state, while the ground state of  $\text{NiO}_2^-$  is determined as the  $\tilde{\chi}^2\Pi_g$  state. The valence orbitals of  $\text{NiO}_2$  are composed of the Ni 4s and 3d orbitals and the O 2s and 2p orbitals, as shown in Fig. 3. The corresponding orbital compositions are summarized in Table 5. The Ni  $3d_{x^2-y^2}$  and  $3d_{xy}$  orbitals together with the O  $2p_x$  and  $2p_y$  orbitals form the  $1\pi_g$  bonding orbitals and the  $2\pi_g$  anti-bonding orbitals. The Ni  $3d_{x^2-y^2}$  and  $3d_{xy}$  orbitals do not mix with oxygen valence orbitals and form the non-bonding  $1\delta_g$  orbitals. The  $2\sigma_g^+$  orbitals consist of contributions from the Ni orbitals and the O 2s and 2p<sub>z</sub> orbitals. The  $1\sigma_g^+$  orbitals are mainly composed of

**Table 1** Peak positions, shifts from peak A1, and assignments, in units of  $\text{cm}^{-1}$ , for the  $\tilde{\chi}^1\Sigma_g^+ \leftarrow \tilde{\chi}^2\Pi_g$  detachment transitions of  $\text{NiO}_2^-$ . Uncertainty in the peak positions correspond to one standard deviation from a Gaussian fit to the highest-resolution experimental trace for each feature

| Peak | eBE        | Shift | Assignment    |
|------|------------|-------|---------------|
| A1   | 24 571(6)  | —     | $0_0^0$       |
| B1   | 24 691(7)  | 120   | $2_0^1$       |
| A2   | 24 815(13) | 244   | $2_0^2$       |
| B2   | 24 936(8)  | 365   | $2_0^3$       |
| A3   | 25 061(12) | 490   | $2_0^4$       |
| B3   | 25 190(7)  | 619   | $2_0^5$       |
| A4   | 25 316(6)  | 745   | $1_0^1$       |
| B4   | 25 442(9)  | 871   | $1_0^1 2_0^1$ |
| A5   | 25 572(9)  | 1001  | $1_0^1 2_0^2$ |
| B5   | 25 700(8)  | 1129  | $1_0^1 2_0^3$ |
| A6   | 25 832(9)  | 1261  | $1_0^1 2_0^4$ |
| B6   | 25 961(7)  | 1390  | $1_0^1 2_0^5$ |
| A7   | 26 065(8)  | 1494  | $1_0^2$       |
| B7   | 26 192(9)  | 1621  | $1_0^2 2_0^1$ |
| B8   | 26 223(7)  | 1652  | $1_0^2 2_0^2$ |
| A8   | 26 356(9)  | 1786  | $1_0^2 2_0^3$ |
| B9   | 26 436(6)  | 1865  | $1_0^2 2_0^4$ |
| B10  | 26 454(7)  | 1883  | $1_0^2 2_0^5$ |
| A9   | 26 529(11) | 1957  | $3_0^2$       |
| B11  | 26 692(9)  | 2121  | $2_0^1 3_0^2$ |
| B12  | 26 716(9)  | 2145  | $1_0^2 2_0^5$ |
| A10  | 26 783(9)  | 2212  | $1_0^3$       |
| B13  | 26 928(10) | 2357  | $1_0^1 2_0^1$ |
| B14  | 26 945(7)  | 2374  | $1_0^2 2_0^1$ |
| B15  | 26 978(7)  | 2406  | $1_0^3 2_0^3$ |
| B16  | 27 187(28) | 2616  | $1_0^2 2_0^9$ |
| A11  | 27 283(35) | 2712  | $1_0^1 3_0^2$ |
| A12  | 27 519(11) | 2948  | $1_0^4$       |
| B17  | 27 660(11) | 3089  | $1_0^4 2_0^1$ |
| A13  | 28 260(11) | 3689  | $1_0^5$       |

**Table 2** Peak positions, shifts from peak C1, and assignments, in units of  $\text{cm}^{-1}$ , for the  $\tilde{\alpha}^3\Pi_g \leftarrow \tilde{\chi}^2\Pi_g$  detachment transitions of  $\text{NiO}_2^-$ . Uncertainty in the peak positions correspond to one standard deviation from a Gaussian fit to the highest-resolution experimental trace for each feature

| Peak | eBE        | Shift | Assignment                    |
|------|------------|-------|-------------------------------|
| C1   | 27 783(3)  | —     | $\tilde{\alpha}^3\Pi_g 0_0^0$ |
| C2   | 27 913(5)  | 131   | $2_0^1$                       |
| C3   | 28 468(11) | 685   | $1_0^1$                       |
| C4   | 28 589(13) | 807   | $1_0^1 2_0^1$                 |
| C5   | 29 162(12) | 1380  | $1_0^2$                       |
| C6   | 29 271(17) | 1488  | $1_0^1 2_0^1$                 |
| C7   | 29 883(9)  | 2100  | $1_0^3$                       |
| C8   | 29 968(15) | 2186  | $1_0^3 2_0^1$                 |

the O 2s and 2p<sub>z</sub> orbitals with a small contribution from the Ni 4s orbitals. The ground state of  $\text{NiO}_2$  takes a closed-shell configuration  $(1\sigma_g^+)^2(1\sigma_u^+)^2(2\sigma_g^+)^2(1\delta_g)^4(3\sigma_g^+)^2(2\sigma_u^+)^2(1\pi_u)^4(1\pi_g)^4(2\pi_g)^0$ , with the anti-bonding 2 $\pi_g$  orbitals left unoccupied. Since the 1 $\sigma_g^+$ , 2 $\sigma_g^+$ , 1 $\delta_g$ , 3 $\sigma_g^+$ , 1 $\pi_g$  orbitals are fully occupied for all electronic states discussed here, we will use the occupation numbers for the 3 $\sigma_g^+$ , 2 $\sigma_u^+$ , 1 $\pi_u$ , and 2 $\pi_g$  orbitals to denote electronic states. In this notation the ground state of  $\text{NiO}_2$  is represented as  $(3\sigma_g^+)^2(2\sigma_u^+)^2(1\pi_u)^4(2\pi_g)^0$ . The ground  $\tilde{\chi}^2\Pi_g$  state

**Table 3** Peak positions, shifts from peak D1, and assignments, in units of  $\text{cm}^{-1}$ , for the  $\tilde{\Lambda}^1\Pi_g \leftarrow \tilde{\chi}^2\Pi_g$  detachment transitions of  $\text{NiO}_2^-$ . Uncertainty in the peak positions correspond to one standard deviation from a Gaussian fit to the highest-resolution experimental trace for each feature

| Peak | eBE        | Shift | Assignment                     |
|------|------------|-------|--------------------------------|
| D1   | 30 557(7)  | —     | $\tilde{\Lambda}^1\Pi_g 0_0^0$ |
| D2   | 30 669(12) | 112   | $2_0^1$                        |
| D3   | 30 814(10) | 257   | $2_0^2$                        |
| D4   | 31 263(19) | 706   | $1_0^1$                        |
| D5   | 31 422(16) | 865   | $1_0^{12} 2_0^1$               |
| D6   | 31 944(9)  | 1275  | $1_0^2$                        |

**Table 4** Experimental parameters for the various states of  $\text{NiO}_2$  probed in this work, extracted from the cryo-SEVI spectra of photodetachment of  $\text{NiO}_2^-$ , along with comparison to our SFX2C-1e-CCSD(T)/aug-cc-pVTZ theoretical calculations for the ground state and EOM-CCSDT/cc-pVQZ calculations for the excited state term energies. Available literature values are presented

| Parameter                  | Calculated                      | SEVI       | Literature            |
|----------------------------|---------------------------------|------------|-----------------------|
| $\tilde{\chi}^1\Sigma_g^+$ | EA (eV)                         | 3.0464(7)  | 3.043(5) <sup>a</sup> |
|                            | $\omega_1$ ( $\text{cm}^{-1}$ ) | 774        | 749 <sup>b</sup>      |
|                            | $\omega_2$ ( $\text{cm}^{-1}$ ) | 135        | 120(7)                |
|                            | $\omega_3$ ( $\text{cm}^{-1}$ ) | 985        | 978(16)               |
| $\tilde{\alpha}^3\Pi_g$    | $T_e$ (eV)                      | 0.3982(7)  | 0.40(2) <sup>c</sup>  |
|                            | $\omega_1$ ( $\text{cm}^{-1}$ ) | 685(11)    |                       |
|                            | $\omega_2$ ( $\text{cm}^{-1}$ ) | 131(5)     |                       |
| $\tilde{\Lambda}^1\Pi_g$   | $T_e$ (eV)                      | 0.7422(10) | 0.77(3) <sup>c</sup>  |
|                            | $\omega_1$ ( $\text{cm}^{-1}$ ) | 706(19)    |                       |
|                            | $\omega_2$ ( $\text{cm}^{-1}$ ) | 112(12)    |                       |

<sup>a</sup> Ref. 11. <sup>b</sup> Ref. 12. <sup>c</sup> Ref. 10.

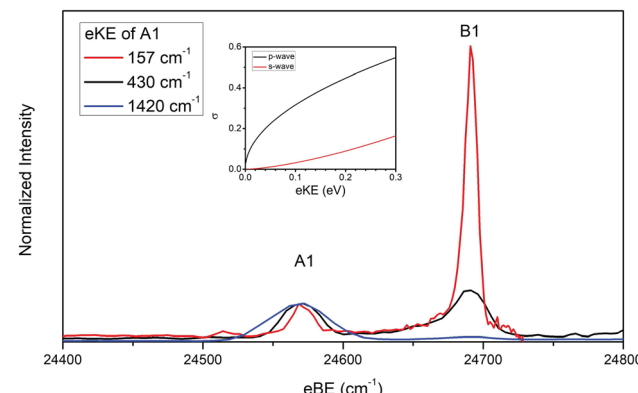


**Fig. 2** Cryo-SEVI spectra of  $\text{NiO}_2^-$  at three photon energies illustrating the differing signal attenuation for features A1 and B1 as eKE decreases. The intensity of each scan has been normalized to feature A1. Photon energies employed are 25 991 (blue), 25 001 (black), and 24 728  $\text{cm}^{-1}$  (red). Insert: photodetachment cross-section as a function of kinetic energy for s- and p-wave detachment as outlined by the Wigner threshold law.<sup>67</sup>

of  $\text{NiO}_2^-$  places the excess electron in the 2 $\pi_g$  orbital, which is expected to weaken the Ni–O bond.

Although the ground state wave function of  $\text{NiO}_2$  is dominated by a closed shell  $(3\sigma_g^+)^2(2\sigma_u^+)^2(1\pi_u)^4(2\pi_g)^0$  configuration,

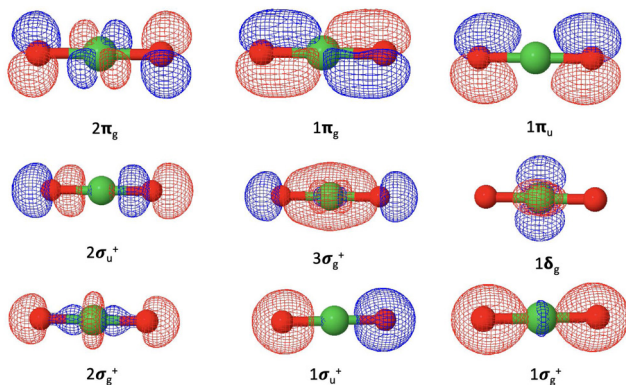


Fig. 3 Valence molecular orbitals of  $\text{NiO}_2$  originating from the Ni 4s and 3d orbitals and the O 2s and 2p orbitals.

Table 5 The principal compositions of valence molecular orbitals of  $\text{NiO}_2$ . Significant secondary contributions are enclosed in the brackets

| Molecular orbitals | Compositions  |
|--------------------|---|
| $1\sigma_g^+$      | O 2s  |
| $1\sigma_u^+$      | O 2s  |
| $2\sigma_g$        | Ni 3d <sub>z2</sub> [O 2s and 2p <sub>z</sub> ]                                   |
| $1\delta_g^+$      | Ni 3d <sub>x2-y2</sub> and 3d <sub>xy</sub>                                       |
| $3\sigma_g^+$      | O 2s, 2p <sub>z</sub> [Ni 4s, 3d <sub>0</sub> ]                                   |
| $2\sigma_u^+$      | O 2s, 2p <sub>z</sub>   |
| $1\pi_u$           | O 2p <sub>x</sub> and 2p <sub>y</sub>   |
| $1\pi_g$           | O 2p <sub>x</sub> and 2p <sub>y</sub> [Ni 3d <sub>xz</sub> and 3d <sub>yz</sub> ] |
| $2\pi_g$           | Ni 3d <sub>xz</sub> and 3d <sub>yz</sub> [O 2p <sub>x</sub> and 2p <sub>y</sub> ] |

this electronic state exhibits strong electron correlation because of the low-lying anti-bonding  $2\pi_g$  orbitals. An analysis in the ESI† shows that CCSD(T) calculations provide reasonably accurate structure and frequencies, in spite of the slow convergence of the CC series. The CCSD(T) results perhaps slightly overestimate the vibrational frequency of the bending mode  $\omega_2$  and underestimate those of the antisymmetric stretching and symmetric stretching modes ( $\omega_3$  and  $\omega_1$ ). The ground state of  $\text{NiO}_2^-$  is dominated by the  $(3\sigma_g^+)^2 (2\sigma_u^+)^2 (1\pi_u)^4 (2\pi_g)^1$  configuration. As discussed in the ESI,† the CCSD(T) results are also reasonably accurate for this electronic state.

We have summarized the adiabatic electron affinity, equilibrium structures, and harmonic frequencies computed at the SFX2C-1e-CCSD(T)/aug-cc-pVTZ level of theory in Table 6 and have utilized these parameters in the FC simulations presented in Fig. 1. As expected, the occupation of an anti-bonding  $2\pi_g$  orbital in  $\text{NiO}_2^-$  significantly increases the Ni–O bond length, *e.g.*, the difference between the Ni–O bond lengths in  $\text{NiO}_2$  and  $\text{NiO}_2^-$  computed at the CCSD(T) level amounts to 0.034 Å. The population of this orbital also reduces the asymmetric stretching frequency of  $\text{NiO}_2^-$  by around 70  $\text{cm}^{-1}$ . The large change in the Ni–O bond length leads to a significant FC progression for the photodetachment transitions from the  $\tilde{\chi}^2\Pi_g$  state of  $\text{NiO}_2^-$  to the  $\tilde{\chi}^1\Sigma_g^+$  of  $\text{NiO}_2$  due to the FC activity of the symmetric stretch  $\omega_1$  ( $\sigma_g$ ) mode, which is responsible for much of the vibrational structure observed in the photoelectron spectrum of  $\text{NiO}_2^-$ .

Table 6 Computed adiabatic electron affinity ( $\text{EA}_a$ ), bond lengths, and harmonic vibrational frequencies for the  $\tilde{\chi}^1\Sigma_g^+$  state of  $\text{NiO}_2$  and the  $\tilde{\chi}^2\Pi_g$  state of  $\text{NiO}_2^-$ . Scalar-relativistic effects have been taken into account using the SFX2C-1e scheme. The aug-cc-pVTZ basis sets recontracted for the SFX2C-1e scheme have been used. Reported values are in  $\text{cm}^{-1}$  except for bond length, which is reported in Å

|                  | $R(\text{Ni–O})$ | $\omega_1$ ( $\sigma_g$ ) | $\omega_2$ ( $\pi_u$ ) | $\omega_3$ ( $\sigma_u$ ) | $\text{EA}_a$ |
|------------------|------------------|---------------------------|------------------------|---------------------------|---------------|
| $\text{NiO}_2$   | 1.609            | 774                       | 135                    | 985                       | 24 523        |
| $\text{NiO}_2^-$ | 1.643            | 772                       | 96                     | 915                       | —             |

Excitation of a  $3\sigma_g^+$ ,  $1\pi_u$  or  $2\sigma_u$  electron into an anti-bonding  $2\pi_g$  orbital gives rise to several low-lying excited states of  $\text{NiO}_2$ . The lowest excited state of  $\text{NiO}_2$  is a  $^3\Pi_g$  state with the leading configuration  $(3\sigma_g^+)^2 (2\sigma_u^+)^2 (1\pi_u)^4 (2\pi_g)^1$ , which resides 0.56 eV above the ground  $\tilde{\chi}^1\Sigma_g^+$  state. The corresponding singlet  $^1\Pi_g$  state lies 0.88 eV above the ground state. Both states can be accessed from the ground  $\tilde{\chi}^2\Pi_g$  state of  $\text{NiO}_2^-$  by detaching a  $3\sigma_g^+$  electron. Meanwhile, the detachment of a  $1\pi_u$  electron or a  $2\sigma_u$  electron leads to a manifold of  $(3\sigma_g^+)^2 (2\sigma_u^+)^2 (1\pi_u)^3 (2\pi_g)^1$  states and a manifold of  $(3\sigma_g^+)^2 (2\sigma_u^+)^1 (1\pi_u)^4 (2\pi_g)^1$  states lying around 1.1 eV and 2 eV above the ground state, respectively. These findings are in good agreement with the MRCI calculations of Hübner,<sup>22</sup> and are outlined in Table S2 (ESI†). Details about the EOM-CC computations for excitation energies are documented in the ESI,†

#### IV.B Ground state Franck–Condon allowed transitions

Table 1 lists the vibrational assignments of features arising from the  $\tilde{\chi}^1\Sigma_g^+ \leftarrow \tilde{\chi}^2\Pi_g$  transition. These assignments are informed by the results of our FC simulations as well as the previously reported photoelectron spectrum of Ramond *et al.*<sup>11</sup> As features A1–13 are largely reproduced in the simulated spectra, they are assigned to Franck–Condon allowed transitions within the  $\tilde{\chi}^1\Sigma_g^+ \leftarrow \tilde{\chi}^2\Pi_g$  photodetachment band of  $\text{NiO}_2$ . FC-allowed transitions include all  $\Delta\nu$  transitions in totally symmetric vibrational modes ( $\sigma_g$  for linear species) and even  $\Delta\nu$  transitions along non-totally symmetric modes.<sup>63</sup>

Most prominent among these features is A1, here assigned as the  $0_0^0$  vibrational origin, allowing for the extraction of a refined electron affinity for  $\text{NiO}_2$  and providing an order of magnitude improvement in the precision of this measurement of 3.0464(7) eV, compared to 3.043(5) eV in ref. 11. The measured EA here is in good agreement with our calculated value of 3.0405 eV.

Beyond the vibrational origin is a wealth of vibrational structure, owing to an extended progression in the  $\nu_1$  symmetric stretch of  $\text{NiO}_2$ , where there  $1_0^1$ ,  $1_0^2$ ,  $1_0^3$ ,  $1_0^4$ , and  $1_0^5$  transitions are observed (A4, A7, A10, A12, A13, respectively). Weak but allowed transitions involving the non-totally symmetric  $\nu_2$  bending and  $\nu_3$  anti-symmetric stretching modes contribute to the remainder of the A-features in this band, with a short progression in the  $\nu_2$  bending coordinate ( $2_0^2$  and  $2_0^4$ , corresponding to A2 and A3, respectively), the appearance of the FC-allowed  $3_0^2$  transition (A9), and several combination bands including A5, A6, and A8 (see Table 1).

From the harmonic progressions along  $\nu_1$  and  $\nu_2$  and the appearance of the  $3_0^2$  transition, we obtain the frequencies of all three vibrational modes of the  $\tilde{X}^1\Sigma_g^+$  state of  $\text{NiO}_2$ . These values,  $\nu_1 = 745(6)$ ,  $\nu_2 = 122(18)$ , and  $\nu_3 = 978(16) \text{ cm}^{-1}$ , are in good agreement with those previously reported from photo-electron spectroscopy ( $\nu_1 = 745(30) \text{ cm}^{-1}$ )<sup>11</sup> and FTIR studies of  $\text{NiO}_2$  in a Ne matrix ( $\nu_1 = 749$  and  $\nu_3 = 977.5 \text{ cm}^{-1}$ )<sup>12</sup>, as well as our calculated values (Table 6) of  $\nu_1 = 774$ ,  $\nu_2 = 135$ , and  $\nu_3 = 985 \text{ cm}^{-1}$ . Further, the observed frequency for the  $\nu_2$  bending mode matches well with an observed but unassigned feature in the Ne matrix data at  $129.9 \text{ cm}^{-1}$ ,<sup>9</sup> suggesting that this peak was from IR excitation of the  $\nu_2$  mode.

#### IV.C Ground state Franck–Condon forbidden transitions

We now consider the assignments to the features in the  $\tilde{X}^1\Sigma_g^+ \leftarrow \tilde{X}^2\Pi_g$  band that are not reproduced by our FC simulations, peaks B1–B17 (Table 1). The spacing of these features is consistently  $\sim 120 \text{ cm}^{-1}$  above that of an allowed transition (as is the case for B1–B9, B13, B17) or  $\sim 240 \text{ cm}^{-1}$  above another “B” feature (as is the case for B9  $\rightarrow$  B11, B10  $\rightarrow$  B12, B12  $\rightarrow$  B14, B13  $\rightarrow$  B15, B14  $\rightarrow$  B16). The similarity of these spacings with that of our measured value for the  $\nu_2$  bending frequency ( $122(18) \text{ cm}^{-1}$ ) suggests these features arise from transitions terminating in odd quanta of the non-totally symmetric  $\nu_2$  mode. We thus assign peaks B1–B17 to transitions of this type to neutral levels with  $\pi_u$  vibrational symmetry.

These transitions are Franck–Condon forbidden but can arise through Herzberg–Teller (HT) coupling to an excited electronic state with the appropriate symmetry.<sup>29,64–66</sup> Briefly, two vibronic states,  $a$  and  $b$ , can mix through HT-coupling provided their electronic and vibrational symmetries  $\Gamma_{\text{elec}}$  and  $\Gamma_{\text{vib}}$ , respectively, satisfy<sup>63</sup>

$$\Gamma_{\text{elec}}^a \otimes \Gamma_{\text{vib}}^a \otimes \Gamma_{\text{elec}}^b \otimes \Gamma_{\text{vib}}^b \supset \Gamma_{\text{TS}} \quad (1)$$

Here  $\Gamma_{\text{TS}}$  is the totally symmetric representation within the molecular point group. This mixing then creates two new states  $|a_0\rangle = c_{1a}|a\rangle + c_{2a}|b\rangle$  and  $|b_0\rangle = c_{1b}|a\rangle + c_{2b}|b\rangle$ , each an admixture of the two zero-order vibronic levels. Thus, if detachment to state  $b$  is FC-allowed, then detachment to state  $a_0$  becomes allowed, but will display the electronic character of state  $b$ .

In the present case, the electronic and vibrational symmetries of the final states in features B1–B17,  $\Gamma_{\text{elec}}^a$  and  $\Gamma_{\text{vib}}^a$ , are  $\Sigma_g^+$  and  $\pi_u$ , respectively. These states can only be observed if they mix with a state  $b$  that is FC-allowed for detachment from the anion, *i.e.*  $\Gamma_{\text{vib}}^b = \sigma_g$ , thereby requiring that the excited electronic state HT-coupled to this state be of  $\Pi_u$  symmetry. Our calculations (Table S2, ESI†) find that such an excited state resides  $2.24 \text{ eV}$  above the neutral ground state.

The presence of vibronic coupling here is affirmed by the differing behavior of the FC-forbidden and FC-allowed features as the photon energy is changed, as shown in Fig. 2. Here, cryo-SEVI spectra are plotted at three photon energies, showing that as the photon energy is lowered and approaches the detachment threshold, the intensity of features A1 and A2 drops precipitously relative to that of B1 and B3. This effect is ascribed to a reduced photodetachment cross section for feature A1 and A3 at low eKE.

Such a difference can be related to the relative scaling of the detachment cross sections at low eKE's, given by the Wigner threshold law:<sup>67</sup>

$$\sigma \propto (\text{eKE})^{l+1/2}, \quad (2)$$

where  $\sigma$  is the detachment cross section and  $l$  is the angular momentum of the detached electron. Thus, photodetachment is suppressed more strongly at low eKE for detachment of higher  $l$  electrons (see inset of Fig. 2), due to the centrifugal barrier experienced by the departing electron.

For detachment to the  $\tilde{X}^1\Sigma_g^+$  state of  $\text{NiO}_2$ , selection rules for molecular photodetachment prohibit detachment of  $l = 0$  electrons, and  $p$ -wave detachment dominates.<sup>68</sup> Conversely, transitions terminating in odd quanta along the  $\nu_2$  normal coordinate do so in a neutral level with a contribution from an excited state of  $\Pi_u$  symmetry, for which detachment can proceed *via*  $l = 0$  (*s*-wave) transitions.

The disparity in near-threshold cross-section between the “A” and “B” features is a tell-tale sign of HT coupling in cryo-SEVI spectra,<sup>29,64–66</sup> as this indicates that “B” features correspond to detachment with lower values of  $l$  than the “A” features, reflecting the electronic character of the  $\Pi_u$  electronic state that lends intensity to these transitions. Consequently, spectra for the “B” peaks can be obtained closer to photodetachment threshold, where cryo-SEVI resolution is improved, leading to narrower features as was observed in the cryo-SEVI spectra of the indenyl and nitrate anions.<sup>66,69</sup> As such, we are able to refine our determined value for the  $\nu_2$  bending mode of  $\text{NiO}_2$  from the position of B1 as  $120(7) \text{ cm}^{-1}$ .

#### IV.D Excited state transitions

Beyond the strongest vibrational transitions in the  $\tilde{X}^1\Sigma_g^+$  manifold reside the strong features C1 and D1. The positions of these features ( $3.4447(4)$  and  $3.7886(9) \text{ eV}$ , respectively) coincide with the previously observed onset of transitions assigned to the  $\tilde{a}^1\Delta_g$  and  $\tilde{b}^1\Sigma_g^+$  states ( $3.45(2)$  and  $3.82(3) \text{ eV}$ , respectively) of  $\text{NiO}_2$  based on a molecular orbital picture.<sup>10</sup> Subsequent theoretical work, however, has determined the low-lying states of  $\text{NiO}_2$  as the  $\tilde{a}^3\Pi_g$  and  $\tilde{A}^1\Pi_g$  states.<sup>22</sup> These assignments agree with our EOM-CC calculations, which find the same state ordering. We thus assign C1 and D1 as the vibrational origins of the  $\tilde{a}^3\Pi_g \leftarrow \tilde{X}^2\Pi_g$  and  $\tilde{A}^1\Pi_g \leftarrow \tilde{X}^2\Pi_g$  transitions, with term energies of  $0.3982(7)$  and  $0.7422(10) \text{ eV}$ , respectively, determined by the shift in peak location from A1. These reported term energies are more precise than those previously reported ( $0.40(2)$  and  $0.77(3) \text{ eV}$ , respectively),<sup>10</sup> and are in good agreement with our computed term energies of  $0.56$  and  $0.88 \text{ eV}$ , validating this reassignment.

Numerous weaker features reside beyond peaks C1 and D1 (C2–C8, D2–D6) that report on the vibrational structure of the  $\tilde{a}^3\Pi_g$  and  $\tilde{A}^1\Pi_g$  excited states (Tables 2 and 3). In the  $\tilde{a}^3\Pi_g$  state, there appears to be a progression of a vibrational feature with a frequency of  $685(11) \text{ cm}^{-1}$  as well as the appearance of the vibrational fundamental and combination bands involving a mode with frequency of  $130(5) \text{ cm}^{-1}$ . Similarly, in the  $\tilde{A}^1\Pi_g$  state, there appear to be two progressions in features with

average spacings of 112(12) and 705(19)  $\text{cm}^{-1}$ . While we do not have theoretical calculations to make definitive assignments to these features, their relative spacing are close to those of the  $\nu_1$  and  $\nu_2$  vibrational modes that dominate the structure in the ground state of spectrum  $\text{NiO}_2$ . We thus tentatively assign the observed structure to activity along the  $\nu_1$  and  $\nu_2$  vibrational modes of  $\text{NiO}_2$  in the  $\tilde{\alpha}^3\Pi_g$  and  $\tilde{\Lambda}^1\Pi_g$  excited states with vibrational frequencies of 685(11) and 130(5)  $\text{cm}^{-1}$  ( $\tilde{\alpha}^3\Pi_g$ ) as well as 705(19) and 112(12)  $\text{cm}^{-1}$  ( $\tilde{\Lambda}^1\Pi_g$ ), respectively (outlined in Table 4).

## Conclusion

Here, we report high-resolution cryo-SEVI spectra of  $\text{NiO}_2^-$  showing photodetachment to the  $\tilde{\chi}^1\Sigma_g^+$ ,  $\tilde{\alpha}^3\Pi_g$ , and  $\tilde{\Lambda}^1\Pi_g$  states of  $\text{NiO}_2$ . In the ground state, we observe FC-allowed transitions involving the  $\nu_1$  symmetric stretch,  $\nu_2$  bending, and  $\nu_3$  anti-symmetric stretch from which we extract vibrational frequencies of  $\nu_1 = 745(6)$ ,  $\nu_2 = 122(18)$ , and  $\nu_3 = 978(16)$   $\text{cm}^{-1}$ , in good agreement with previously reported values. These assignments are facilitated by FC simulations using the SFX2C-1e-CCSD(T)/aug-cc-pVTZ geometries and vibrational frequencies for  $\text{NiO}_2^{0/-}$ . Notably, we observe extended FC-forbidden progressions to final states with odd quanta in the  $\nu_2$  bending coordinate that we ascribe to vibronic coupling to the  $\Pi_u$  excited state of  $\text{NiO}_2$ , calculated to reside 2.24 eV above the ground state. From the onset of structure in the ground and excited states, we are able to refine the electron affinity and term energies of  $\text{NiO}_2$  and its first two excited states (EA = 3.0464(7) eV,  $T_e(\tilde{\alpha}^3\Pi_g) = 0.3982(7)$  eV,  $T_e(\tilde{\Lambda}^1\Pi_g) = 0.7422(10)$  eV), in good agreement with our calculated values.

## Conflicts of interest

There are no conflicts to declare.

## Acknowledgements

The research conducted at UC Berkeley is funded by the Air Force Office of Scientific Research under Grant No. FA9550-19-1-0051 and the work done at Johns Hopkins University is supported by Department of Energy Early Career Research Program under Award Number DE-SC0020317. M. C. B. thanks the Army Research Office for a National Defense Science and Engineering Graduate fellowship. J. A. L. thanks the Alexander von Humboldt Foundation for a Feodor Lynen Research Fellowship.

## References

- 1 N. A. K. Aramouni, J. G. Touma, B. Abu Tarboush, J. Zeaiter and M. N. Ahmad, *Renewable Sustainable Energy Rev.*, 2018, **82**, 2570–2585.
- 2 C. Alvarez-Galvan, M. Melian, L. Ruiz-Matas, J. L. Eslava, R. M. Navarro, M. Ahmadi, B. Roldan Cuenya and J. L. G. Fierro, *Front. Chem.*, 2019, **7**, 104.
- 3 E. Heracleous, A. F. Lee, K. Wilson and A. A. Lemonidou, *J. Catal.*, 2005, **231**, 159–171.
- 4 Y. L. Zhou, F. F. Wei, J. Lin, L. Li, X. Y. Li, H. F. Qi, X. L. Pan, X. Y. Liu, C. D. Huang, S. Lin and X. D. Wang, *ACS Catal.*, 2020, **10**, 7619–7629.
- 5 S. Dey, G. C. Dhal, D. Mohan and R. Prasad, *Adv. Compos. Hybrid Mater.*, 2019, **2**, 626–656.
- 6 A. W. Castleman, *Catal. Lett.*, 2011, **141**, 1243–1253.
- 7 J. L. Mason, C. N. Folluo and C. C. Jarrold, *J. Chem. Phys.*, 2021, **154**, 200901.
- 8 H. Huber and G. A. Ozin, *Can. J. Chem.*, 1972, **50**, 3746–3747.
- 9 A. Citra, G. V. Chertihin, L. Andrews and M. Neurock, *J. Phys. Chem. A*, 1997, **101**, 3109–3118.
- 10 H. B. Wu and L. S. Wang, *J. Chem. Phys.*, 1997, **107**, 16–21.
- 11 T. M. Ramond, G. E. Davico, F. Hellberg, F. Svedberg, P. Salen, P. Soderqvist and W. C. Lineberger, *J. Mol. Spectrosc.*, 2002, **216**, 1–14.
- 12 F. Allouti, L. Manceron and M. E. Alikhani, *Phys. Chem. Chem. Phys.*, 2006, **8**, 448–455.
- 13 W. D. Vann, R. L. Wagner and A. W. Castleman, *J. Phys. Chem. A*, 1998, **102**, 1708–1718.
- 14 M. C. Oliveira, J. Marcalo, M. C. Vieira and M. A. A. Ferreira, *Int. J. Mass Spectrom.*, 1999, **185**, 825–835.
- 15 J. U. Reveles, G. E. Johnson, S. N. Khanna and A. W. Castleman, *J. Phys. Chem. C*, 2010, **114**, 5438–5446.
- 16 C. Salvitti, M. Rosi, F. Pepi, A. Troiani and G. de Petris, *Chem. Phys. Lett.*, 2021, **776**, 138555.
- 17 M. R. A. Blomberg, E. M. Siegbahn and A. Strich, *Chem. Phys.*, 1985, **97**, 287–301.
- 18 C. W. Bauschlicher, *J. Phys. Chem. A*, 2004, **108**, 2871–2873.
- 19 K. Deng, J. L. Yang and Q. S. Zhu, *J. Chem. Phys.*, 2003, **118**, 6868–6873.
- 20 G. L. Gutsev, B. K. Rao and P. Jena, *J. Phys. Chem. A*, 2000, **104**, 11961–11971.
- 21 E. L. Uzunova, H. Mikosch and G. S. Nikolov, *J. Chem. Phys.*, 2008, **128**, 094307.
- 22 O. Hubner and H. J. Himmel, *J. Phys. Chem. A*, 2012, **116**, 9181–9188.
- 23 D. M. Neumark, *J. Phys. Chem. A*, 2008, **112**, 13287–13301.
- 24 M. L. Weichman and D. M. Neumark, *Annu. Rev. Phys. Chem.*, 2018, **69**, 101–124.
- 25 A. Osterwalder, M. J. Nee, J. Zhou and D. M. Neumark, *J. Chem. Phys.*, 2004, **121**, 6317–6322.
- 26 C. Hock, J. B. Kim, M. L. Weichman, T. I. Yacovitch and D. M. Neumark, *J. Chem. Phys.*, 2012, **137**, 244201.
- 27 U. Even, J. Jortner, D. Noy, N. Lavie and C. Cossart-Magos, *J. Chem. Phys.*, 2000, **112**, 8068–8071.
- 28 J. B. Kim, C. Hock, T. I. Yacovitch and D. M. Neumark, *J. Phys. Chem. A*, 2013, **117**, 8126–8131.
- 29 J. A. DeVine, M. L. Weichman, B. Laws, J. Chang, M. C. Babin, G. Balerdi, C. J. Xie, C. L. Malbon, W. C. Lineberger, D. R. Yarkony, R. W. Field, S. T. Gibson, J. Y. Ma, H. Guo and D. M. Neumark, *Science*, 2017, **358**, 336–339.

30 M. C. Babin, J. A. DeVine, M. L. Weichman and D. M. Neumark, *J. Chem. Phys.*, 2018, **149**, 174306.

31 W. C. Wiley and I. H. McLaren, *Rev. Sci. Instrum.*, 1955, **26**, 1150–1157.

32 A. T. J. B. Eppink and D. H. Parker, *Rev. Sci. Instrum.*, 1997, **68**, 3477–3484.

33 D. W. Chandler and P. L. Houston, *J. Chem. Phys.*, 1987, **87**, 1445–1447.

34 M. B. Doyle, C. Abeyasera and A. G. Suits, NuACQ, <http://faculty.missouri.edu/suitsa/NuAqc.html>.

35 E. W. Hansen and P. L. Law, *J. Opt. Soc. Am. A*, 1985, **2**, 510–520.

36 C. Blondel, C. Delsart and F. Goldfarb, *J. Phys. B: At. Mol. Phys.*, 2001, **34**, L281–L288.

37 K. Raghavachari, G. W. Trucks, J. A. Pople and M. Head-Gordon, *Chem. Phys. Lett.*, 1989, **157**, 479–483.

38 K. G. Dyall, *J. Chem. Phys.*, 2001, **115**, 9136–9143.

39 W. J. Liu and D. L. Peng, *J. Chem. Phys.*, 2009, **131**, 031104.

40 T. H. Dunning, *J. Chem. Phys.*, 1989, **90**, 1007–1023.

41 R. A. Kendall, T. H. Dunning and R. J. Harrison, *J. Chem. Phys.*, 1992, **96**, 6796–6806.

42 N. B. Balabanov and K. A. Peterson, *J. Chem. Phys.*, 2005, **123**, 064107.

43 G. D. Purvis and R. J. Bartlett, *J. Chem. Phys.*, 1982, **76**, 1910–1918.

44 J. Noga and R. J. Bartlett, *J. Chem. Phys.*, 1987, **86**, 7041–7050.

45 G. E. Scuseria and H. F. Schaefer, *Chem. Phys. Lett.*, 1988, **152**, 382–386.

46 S. A. Kucharski and R. J. Bartlett, *Theor. Chim. Acta*, 1991, **80**, 387–405.

47 N. Olyphant and L. Adamowicz, *J. Chem. Phys.*, 1991, **95**, 6645–6651.

48 J. Gauss, J. F. Stanton and R. J. Bartlett, *J. Chem. Phys.*, 1991, **95**, 2623–2638.

49 J. F. Stanton, J. Gauss, J. D. Watts and R. J. Bartlett, *J. Chem. Phys.*, 1991, **94**, 4334–4345.

50 J. D. Watts, J. Gauss and R. J. Bartlett, *Chem. Phys. Lett.*, 1992, **200**, 1–7.

51 L. Cheng and J. Gauss, *J. Chem. Phys.*, 2011, **135**, 084114.

52 D. A. Matthews and J. F. Stanton, *J. Chem. Phys.*, 2015, **142**, 064108.

53 D. A. Matthews, L. Cheng, M. E. Harding, F. Lipparini, S. Stopkowicz, T. C. Jagau, P. G. Szalay, J. Gauss and J. F. Stanton, *J. Chem. Phys.*, 2020, **152**, 214108.

54 D. A. Matthews, *J. Chem. Theory Comput.*, 2020, **16**, 6195–6206.

55 J. G. J. F. Stanton, L. Cheng, M. E. Harding, D. A. Matthews, P. G. Szalay, CFOUR, coupled-cluster techniques for computational chemistry, a quantum-chemical program package, with contributions from, A. A. Auer, R. J. Bartlett, U. Benedikt, C. Berger, D. E. Bernholdt, S. Blaschke, Y. J. Bomble, S. Burger, O. Christiansen, D. Datta, F. Engel, R. Faber, J. Greiner, M. Heckert, O. Heun, M. Hilgenberg, C. Huber, T.-C. Jagau, D. Jonsson, J. Jusélius, T. Kirsch, K. Klein, G. M. Kopper, W. J. Lauderdale, F. Lipparini, T. Metzroth, L. A. Mück, T. Nottoli, D. P. O'Neill, D. R. Price, E. Prochnow, C. Puzzarini, K. Ruud, F. Schiffmann, W. Schwalbach, C. Simmons, S. Stopkowicz, A. Tajti, J. Vázquez, F. Wang, J. D. Watts and the integral packages MOLECULE (J. Almlöf and P. R. Taylor), PROPS (P. R. Taylor), ABACUS (T. Helgaker, H. J. Aa. Jensen, P. Jørgensen, and J. Olsen) and ECP routines by, A. V. Mitin and C. van Wüllen, For the current version, see (<http://www.cfour.de>).

56 S. M. Rabidoux, V. Eijkhout and J. F. Stanton, *J. Chem. Theory Comput.*, 2016, **12**, 728–739.

57 J. F. Stanton and R. J. Bartlett, *J. Chem. Phys.*, 1993, **98**, 7029–7039.

58 K. Kowalski and P. Piecuch, *J. Chem. Phys.*, 2001, **115**, 643–651.

59 S. A. Kucharski, M. Wloch, M. Musial and R. J. Bartlett, *J. Chem. Phys.*, 2001, **115**, 8263–8266.

60 M. Kallay and P. R. Surjan, *J. Chem. Phys.*, 2001, **115**, 2945–2954.

61 M. Kallay and J. Gauss, *J. Chem. Phys.*, 2004, **121**, 9257–9269.

62 M. Kallay, P. R. Nagy, D. Mester, Z. Rolik, G. Samu, J. Csontos, J. Csoka, P. B. Szabo, L. Gyevi-Nagy, B. Hegely, I. Ladjanszki, L. Szegedy, B. Ladočzki, K. Petrov, M. Farkas, P. D. Mezei and A. Ganyecz, *J. Chem. Phys.*, 2020, **152**, 074107.

63 G. Herzberg, *Electronic spectra and electronic structure of polyatomic molecules*, Van Nostrand Reinhold Company, Princeton, NJ, 1966.

64 J. A. DeVine, A. Abou Taka, M. C. Babin, M. L. Weichman, H. P. Hratchian and D. M. Neumark, *J. Chem. Phys.*, 2018, **148**, 222810.

65 M. L. Weichman, L. Cheng, J. B. Kim, J. F. Stanton and D. M. Neumark, *J. Chem. Phys.*, 2017, **146**, 224309.

66 M. C. Babin, J. A. DeVine, M. DeWitt, J. F. Stanton and D. M. Neumark, *J. Phys. Chem. Lett.*, 2020, **11**, 395–400.

67 E. P. Wigner, *Phys. Rev.*, 1948, **73**, 1002–1009.

68 K. J. Reed, A. H. Zimmerman, H. C. Andersen and J. I. Brauman, *J. Chem. Phys.*, 1976, **64**, 1368–1375.

69 J. B. Kim, M. L. Weichman, T. I. Yacovitch, C. Shih and D. M. Neumark, *J. Chem. Phys.*, 2013, **139**, 104301.